

Texture Analysis of Seabed Images: Quantifying the Presence of *Posidonia Oceanica* at Palma Bay

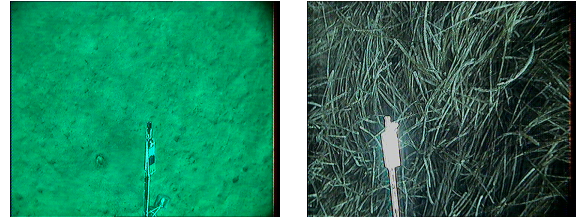
Miquel Massot-Campos, Gabriel Oliver-Codina, Laura Ruano-Amengual and Margaret Miró-Julíá
Departament de Matemàtiques i Informàtica, Universitat de les Illes Balears
Cra. Valldemossa, km. 7,5 07122 Palma de Mallorca (Spain)
Email: {miquel.massot,goliver,margaret.miro}@uib.es

Abstract—An automatic classifier algorithm has been designed to assess the population of *Posidonia oceanica* over a set of underwater images at Palma Bay. Law's energy filters and statistical descriptors of the Gray Level Co-occurrence Matrix have been used to correctly classify the input image patches in two classes: *Posidonia oceanica* or not *Posidonia oceanica*. The input images have been first preprocessed and splitted in three different patch sizes in order to find the best patch size to better classify this seagrass. From all the attributes obtained in these patches, a best subset algorithm has been run to choose the best ones and a decision tree classifier has been trained. The classifier was made by training a Logistic Model Tree from 125 pre-classified images. This classifier was finally tested on 100 new images. The classifier outputs gray level images where black color indicates *Posidonia oceanica* presence and white no presence. Intermediate values are obtained by overlapping the processed patches, resulting in a smoother final result. This images can be merged in an offline process to obtain density maps of this algae in the sea.

I. INTRODUCTION

Posidonia Oceanica (PO) is an endemic seagrass species of the Mediterranean sea that forms large meadows on seabeds up to 40 m deep. The presence of PO is very important to the underwater ecosystem and to the industry developed in the coastal areas, specially tourism and fishing activity, because its profusion is strongly related to biodiversity and water quality of the environment. Unfortunately, the habitat of PO is declining due to anthropogenic impacts (eutrophication, uncontrolled anchoring, trawling, shoreline change) [1] and large-scale changes (increased temperature, biological invasions, among others) [2]. Because of its slow growth and recovery, losses may be irreversible. Thus, regular mapping of PO communities plays an important role in its conservation monitoring [3], [4].

Traditionally, scuba divers in a process that is dangerous, slow, tedious, expensive and imprecise, carry out the above-mentioned survey task. More recent technologies, using sensorized and equipped structures [5]–[7] or even from satellites [8], overcome these problems. One of these platforms has been developed by the *Instituto Mediterráneo de Estudios Avanzados* (IMEDEA) in the last years [9]. This underwater platform is equipped so it can take images at a fixed distance from the seabed and with almost similar illumination conditions. Moreover, the images are located using the GPS data of the supply boat from where the platform is being deployed. Using



(a) No posidonia present, all sand. (b) All posidonia.

Figure 1. Extract of photos.

this system, more than 3.000 georeferenced images (some samples are shown in figure 1), were taken in Palma Bay (Mallorca, ES).

Remotely Operated Vehicles (ROVs) have already been used to achieve this task [6]. Thus, the next technological step would be using Autonomous Underwater Vehicles (AUVs) carrying the operation of surveying and classifying the incoming data in their corresponding class or label. With as little as an onboard camera and the needed thrusters to move, even a simple robot could overcome the scuba divers problems above mentioned. This manuscript presents an objective and automatic way to assess the presence of PO on the mentioned images. Thanks to that, the monitoring process can be extended to consider denser sampling of the PO meadows and longer temporal series. Thus, map generation [10] and recovery studies [1] could be guided by the results of our proposal.

In section II the image preprocess will be explained. With these preprocessed images, several models have been trained using different attributes, which are explained in section III. The chosen model is also described, whilst the experimental results from this model are explained in section IV. Finally, in section V conclusions and further work are presented.

II. PREPROCESS

The images used in this study were provided by IMEDEA, and were captured using a analogic RGB camera housed in a watertight case. The original image size is 720×576 pixel and presents vignetting and a color calibration pattern that was physically placed when the photos were taken (see figure 2). Even with the presence of the color calibration pattern, the photographs lack a correct color balance and contrast. Moreover, to prevent possible errors in the algorithms caused by the presence of the calibration pattern, the process has been restricted to the higher part of the image. Finally, the

This work has been partially supported by the Ministry of Education of Spain (FPI grant BES-2012-054352), the Balear Government (ref 71/2011), FEDER funds and by the European Commission's FP7 under grant agreement 248497 (TRIDENT Project).

useful resolution of the images became 650×300 pixels. The preprocess involves also the conversion of the input photos to black and white. For instance, the resultant preprocess of image 2 is image 3.

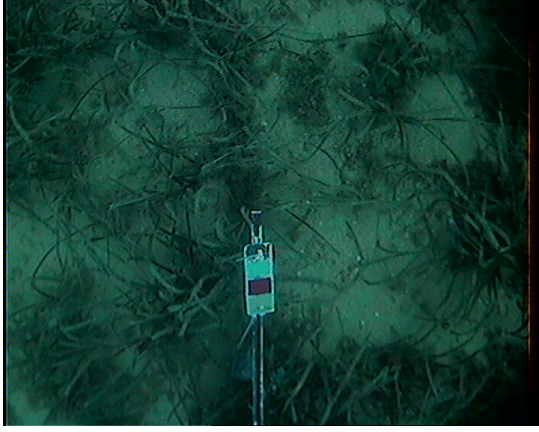


Figure 2. Original size input image. Note the color calibration pattern and the plumb, as well as the left and right black frame and the vignetting.

Next, each image is split in several non-overlapping subimages or patches. These subimages are later used to calculate several values to train the classifier. The size of these subimages has been chosen to be 25×25 , 50×50 and 75×75 , generating three different subimage databases. Some patches can be seen in figure 4. These sets will be referenced from now on as A, B and C. Note that the A set will have more examples than the C because the amount of 75×75 subimages present in one whole image are lower than the number of 25×25 subimages.

In order to describe these images, Law's energy measurements and grey level co-occurrence matrix [11] will be used to identify the differences in texture. These patches will be classified in a binary class: a patch will be either PO or not PO. In the case of Palma Bay photographs, not PO is sand and little pebbles. The identification of other types of seabed (rocks, other algae) is out of the focus of this work.

As each image is split in subimages, each subimage can be classified in one or another class, leading to a resultant global classified image that is not binary. The result classification of the whole image is

$$s = \frac{\sum_P k_i}{\sum_{P \cup N} k_i} \quad (1)$$

where k_i is the classification of the i -th patch of the image, P is the subset of patches classified as PO and N is the subset of patches classified as not PO. Note that $k_i \in P \cup N$ are all the patches in the image. The classification is done at patch level, but the results can be interpreted at both image level and patch level. In section IV both interpretations are discussed.

A. Law's energy measurements

Texture filters like Law's energy measurements can be applied to the input images to create filtered images from which texture features are computed.

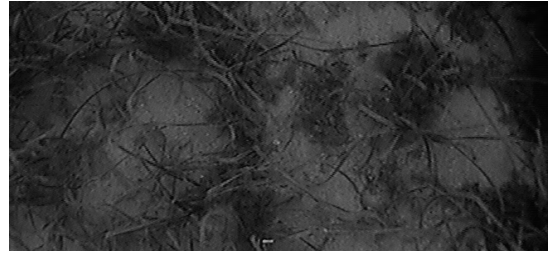


Figure 3. Preprocessed input image.

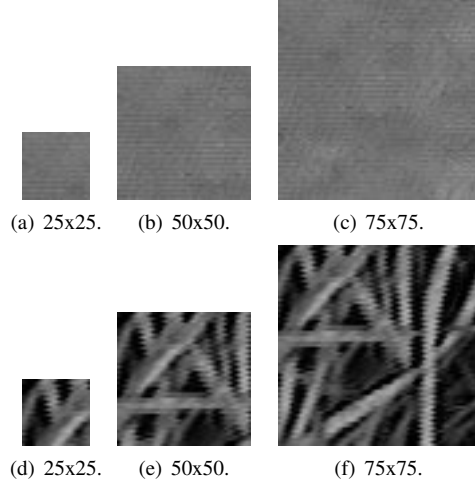


Figure 4. Sand and posidonia patch sizes.

The Law's algorithm first filters the input image using texture filters that will be later explained. Then it computes the texture energy by summing the absolute value of filtering results in local neighbourhoods around each pixel. To obtain rotational invariance, two filters can be combined by applying one filter on the other's result.

Law's texture filters are made from three different vectors convoluted with themselves to create five different new vectors:

$$\begin{aligned} L_5 &= \begin{bmatrix} 1, & 4, & 6, & 4, & 1 \end{bmatrix} \quad (\text{Level}) \\ E_5 &= \begin{bmatrix} -1, & -2, & 0, & 2, & 1 \end{bmatrix} \quad (\text{Edge}) \\ S_5 &= \begin{bmatrix} -1, & 0, & 2, & 0, & -1 \end{bmatrix} \quad (\text{Spot}) \\ W_5 &= \begin{bmatrix} -1, & 2, & 0, & -2, & 1 \end{bmatrix} \quad (\text{Wave}) \\ R_5 &= \begin{bmatrix} 1, & -4, & 6, & -4, & 1 \end{bmatrix} \quad (\text{Ripple}) \end{aligned} \quad (2)$$

L_5 returns a local centered average by convolving the neighbour pixels with a gaussian, E_5 responds to edges by applying a gradient mask, S_5 responds to spots, W_5 responds to wave-like shapes and R_5 to ripples in the texture.

Convolving different 5-pixel long vectors, other lengths can be obtained. In this paper, 5 pixel, 9-pixel and 17-pixel have been considered due to the different subimage size. Depending on the size of the texture to study, a determined vector size is preferred. For example, L_9 can be created as stated in equation 3.

$$\begin{aligned} L_9 &= \text{conv}(L_5, L_5) \\ &= [1, 8, 28, 56, 70, 56, 28, 8, 1] \end{aligned} \quad (3)$$

Then, if every 1D-vector is multiplied with another

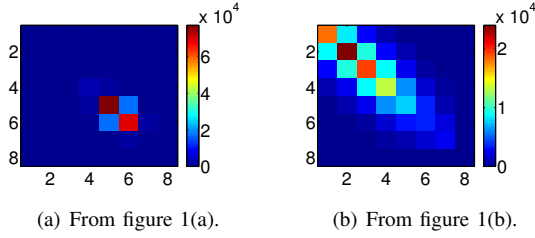


Figure 5. Different GLCM.

one, 25 5×5 kernels or 2D-masks can be obtained ($L_5L_5, L_5E_5, L_5S_5, \dots$).

$$L_5L_5 = L_5^T \cdot L_5 = \begin{pmatrix} 1 & 4 & 6 & 4 & 1 \\ 1 & 16 & 24 & 16 & 4 \\ 6 & 24 & 36 & 24 & 6 \\ 4 & 16 & 24 & 16 & 4 \\ 1 & 4 & 6 & 4 & 1 \end{pmatrix} \quad (4)$$

The same procedure is made with 9×9 and 17×17 sizes, obtaining a total of $25 + 25 + 25$ different matrices

These 75 matrices will be convolved with the subimages. From each of these resulting matrices the average (μ), standard deviation (σ), average of positives (μ^+) and average of negatives (μ^-) are calculated, generating a total of $4 \cdot 75 = 300$ descriptors per subimage.

B. Grey Level Co-occurrence Matrix

On the other hand, Grey Level Co-occurrence Matrix (GLCM) is a tabulation of how often different combinations of pixel brightness values (grey levels) occur in an image. GLCM is obtained from each of the subimages by calculating the frequency rate of neighbor pixel values. In this paper, GLCM has been computed considering 8 bins. From that matrix the attributes listed in table I are obtained, generating a total of 14 descriptors per instance.

These basic statistic descriptors give significant information on how the shape of the GLCM is. If this matrix has almost all values in a small neighborhood means that pixel values are close together, and therefore means that the image contrast is poor and its standard deviation is high. Different configurations exist on these several descriptors chosen. What is more interesting is seeing which values will the classifier finally choose as the best ones to classify. To show these differences, two images have been chosen as examples, one containing sand in figure 5(a) and the other containing PO in figure 5(b). The differences between the two GLCM are evident, and easy to identify with these simple statistical attributes.

III. SELECTION OF ATTRIBUTES AND TRAINING

The method proposed to assess the population of PO in an image is based on texture analysis and machine learning algorithms. First, a training dataset has to be correctly hand-labelled and preprocessed in order to train a specific model. Several models can be trained from different classifier types (trees, perceptron, Bayes, etc.) In this project, C4.5 decision tree, Logistic Model Tree (LMT), Random forest tree (RF), and Multilayer Perceptron classifiers (MP) have been compared to select the best suited classifier for the task.

Table I. VALUES CALCULATED FOR EACH PATCH.

Average	$\mu = \frac{1}{NM} \sum_{i,j=0}^{N,M} P_{i,j}$
Variance	$\sigma^2 = \sum_{i,j=0}^{N,M} (P_{i,j} - \mu)^2$
Standard deviation	$\sigma = \sqrt{\sigma^2}$
Contrast	$Con = \sum_{i,j=0}^{N,M} P_{i,j} (i - j)^2$
Entropy	$Ent = \sum_{i,j=0}^{N,M} P_{i,j} (-\ln(P_{i,j}))$
Homogeneity	$Hom = \sum_{i,j=0}^{N,M} \frac{P_{i,j}}{(i-j)^2}$
Angular Second Moment	$ASM = \sum_{i,j=0}^{N,M} P_{i,j}^2$
Energy	$E = \sqrt{ASM}$
Skew	$Skw = \sum_{i,j=0}^{N,M} \frac{(P_{i,j} - \mu)^3}{\sigma^3}$
Kurtosis	$Kur = \sum_{i,j=0}^{N,M} \frac{(P_{i,j} - \mu)^4}{\sigma^4}$
Maximum probability	$max_i = \max_{i \in N} (P_{i,j})$ $max_j = \max_{j \in M} (P_{i,j})$
GLCM Mean	$\mu_i = \sum_{i,j=0}^{N,M} i(P_{i,j})$ $\mu_j = \sum_{i,j=0}^{N,M} j(P_{i,j})$
GLCM Variance	$\sigma_i^2 = \sum_{i,j=0}^{N,M} P_{i,j} (i - \mu_i)^2$ $\sigma_j^2 = \sum_{i,j=0}^{N,M} P_{i,j} (j - \mu_j)^2$
GLCM Correlation	$\sigma_{ij}^2 = \sum_{i,j=0}^{N,M} P_{i,j} \frac{(i - \mu_i)(j - \mu_j)}{\sqrt{(\sigma_i^2)(\sigma_j^2)}}$

Table II. CORRECTLY CLASSIFIED INSTANCES AND (NUMBER OF ATTRIBUTES USED).

Classifier	Dataset A	Dataset B	Dataset C
C4.5	98,12% (8)	98,61% (2)	99,54% (1)
Logistic Model Tree	98,71% (7)	99,40% (2)	99,07% (2)
Random Forest	97,02% (2)	95,83% (2)	99,07% (1)
Multilayer Perceptron	98,86% (8)	99,40% (3)	99,07% (2)

Once the best model is chosen, the best attribute subset for that model will be determined. In order to select the model, all the texture attributes have been considered in 12 images, six containing PO and six containing sand. These images are used to train the four models using 10 fold cross-validation with Weka [12]. The labeled images are first preprocessed as stated in Section II to obtain a valid text file input for Weka. The best classifier was chosen by selecting the one with the best number of correctly classified instances and the least number of attributes in the three datasets. Greedy Stepwise method was used to find the best subset of attributes for a given classifier. The results of these tests are shown in table II. In that table, Random Forest classifier is shown as the classifier that used the least number of attributes, whilst Multilayer Perceptron and C4.5 the ones that used the most. Logistic Model Tree classifier used almost the same number of attributes as Random forest, but its classification rate is better than the latter.

Therefore, the work has been focused in one classifier. The Logistic Model Tree (LMT) classifier [13] has been chosen for its simplicity and good classification rate. With only one classifier, it is easier to find the best subset of attributes for the whole datasets. Although for dataset C, model C4.5 has better classification rate, LMT achieves better rates in A and B datasets, and is also faster classifying than Multilayer Perceptron. Future works could also explore C4.5 in C dataset.

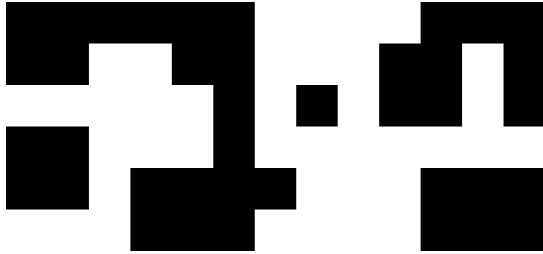
The next step is the selection of the best attributes. These



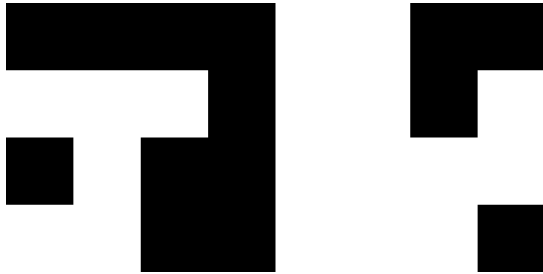
(a) Labeled image from figure 3 used to train the classifier.



(b) Binarized labeled image at 25x25.



(c) Binarized labeled image at 50x50.



(d) Binarized labeled image at 75x75.

Figure 6. Sand and posidonia patch sizes.

attributes have to correctly describe the texture without over fitting the model. Six different training datasets have been used to test the different attributes, grouped in pairs. The first three datasets contain 50 full posidonia and 50 full sand images in three subimage sizes. The other three training datasets contain the abovementioned datasets with an addition of 25 mixed sand and posidonia images in the same subimage sizes. These new 25 images have been previously classified and labelled by a human operator. The dataset pairs are then the dataset with or without these 25 new images, which will be referenced as Training set A for the A-sized training set with 100 images, and Training set A' for the A-sized training set with 125 images.

As an example, the prior labelling of the mixed image in figure 3 is shown in figure 6(a). This hand-labelled image has been binarized in the tree different patch sizes in order to correctly train the classifier. These three binarized training images can be seen in figure 6.

Table III. LIST OF ATTRIBUTES SELECTED AS THE BEST SUBSET OF LMT CLASSIFICATION MODEL.

Attributes selected in	List of attributes
All subsets	Entropy, μ_{L5L5} , μ_{E9L9} , σ_{E5R5} , σ_{R9L9}
Five subsets	σ , μ_{L9L9} , μ_{L17S17} , σ_{E17W17}
Four subsets	\max_i , μ_{L17L17} , μ_{L5W5} , μ_{L17W17} , σ_{L9R9} , σ_{E17S17} , μ_{E5W5} , μ_{W5L5}

Table IV. MODEL A CROSS TRAINING RESULTS. NUMBER OF CORRECTLY CLASSIFIED INSTANCES.

train \ test	A	A'
A	97,07%	93,73%
A'	97,10%	93,74%

The best attribute subset has been obtained for each of the six sets with a best subset attribute selection algorithm [14]. By comparing the common and non common selected attributes, the correlated attributes can be rejected and the most important are kept. The list of the selected attributes is shown in table III.

The most important attributes are: entropy, L_5L_5 average (μ_{L5L5}), E_9L_9 average (μ_{E9L9}) and R_9L_9 standard deviation (σ_{R9L9}). Entropy is high in an homogeneous scene and low in a inhomogeneous scene, L_5L_5 is similar to a Gaussian kernel, so the convolution of a patch with this kernel blurs the input subimage, mixing the corresponding gray values. Moreover, E_9L_9 and R_9L_9 kernels compute texture filters that react to texture in different ways so that the PO is easier to identify.

From these attributes, six LMT models for the six datasets are trained. The pairs are used to validate the models by testing one dataset in the trained model pair. The results of these tests are shown in tables IV, V and VI. Notice in these tables that the number of correctly classified instances is almost the same when the test datasets are changed for the same train set. The addition of examples also drops about a 5% the result, as the mixed images are more difficult to classify. But these numbers confirm that the addition of mixed images, where posidonia and sand appear together, does not drive the classifier to make more mistakes. So the chosen models are A', B' and C', as they contain more examples with the same ability to classify correctly. The results of the 10 fold cross-validation for A', B' and C' models can be seen in table VII.

IV. EXPERIMENTAL RESULTS

Once the three models have been trained, test datasets can be used to verify the classification rates. These datasets are composed of new images which will also be preprocessed like with the training images. However the patches will overlap in order to obtain a refined classification result. For A' the patch size was 25×25 px, and the overlap has been defined as half the size of the patch: 12 px. The same operation is made with the other two sizes. For instance, the classification results of the figure 3 are the three images in figure 7.

An image cannot be classified entirely as belonging exclusively to one class (100% or 0% PO) since there may be intermediate levels of posidonia in there. Also, it is interesting to consider this approach as the classifier could be used to generate PO maps of the surveyed area. To this end, the overlapping results in a new kind of output classification. The

Table V. MODEL B CROSS TRAINING RESULTS. NUMBER OF CORRECTLY CLASSIFIED INSTANCES.

train \ test	B	B'
B	98,87%	95,94%
B'	98,70%	95,77%

Table VI. MODEL C CROSS TRAINING RESULTS. NUMBER OF CORRECTLY CLASSIFIED INSTANCES.

train \ test	C	C'
C	99,30%	96,75%
C'	99,30%	96,58%

classified images have light grey colored patches where the classification has resolved that this particular patch is PO. In the case that the classifier resolves that it is not PO, the resulting image remains white. As the patches overlap, the color becomes darker until it is totally black. For a central patch, up to four overlaps can occur. This results in four levels of PO in a quarter patch: 0%, 33%, 66% and 100% PO confidence. In case the overlap was defined in a different size (for example, instead of taking subimages each 12 pixels when 25×25 patch size is used, the subimages were taken at each pixel) the resulting gray levels would be smoother than only with four.

This overlap is different at the corners of the image, where there are parts of the resultant classification image that are only looked up by one patch. In these cases, the full patch has been considered to be all PO if the corresponding patch was classified in PO class or 0% PO if it belonged to the other class. This way the corners are either white or black, with no gray levels laying between them.

These models are now tested on a new dataset containing 50 PO images and 50 non PO images from the same photography database of Palma Bay. The results will be first presented in terms of image classification, and then in terms of subimage classification. This way, the correctly classified ratio as well as the false positive or the false negative rate will be different, but will allow the lecturer to appreciate how the classification process works.

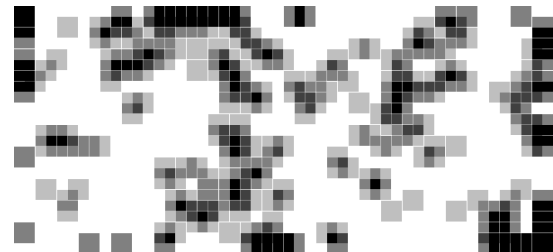
The test images are known a priori, there are 50 which contain PO exclusively and 50 that do not. This particular knowledge allows the classification process to test not only the behaviour and the correctness of the classifier at a subimage level but also to have a global perspective at the whole image. The results of the classification of this database with the three models can be seen in table VIII. Note that the correctly classified instance percentage increases with the patch size, like the original model did when it was trained. This indicates that the C' model classifies better than A' . The results can be also seen at each image. In figure 8 the different classification result is graphed for each non PO image and for the different models, and in figure 9 the remaining 50 PO images are also shown.

When it comes to image classification rates, see the figures 8 and 9, it can be seen that those classification results lead directly to a clear classification in PO or in not PO, but when it comes to patch classification, the rates are different. In fact, the classification results shown in table VIII are patch results.

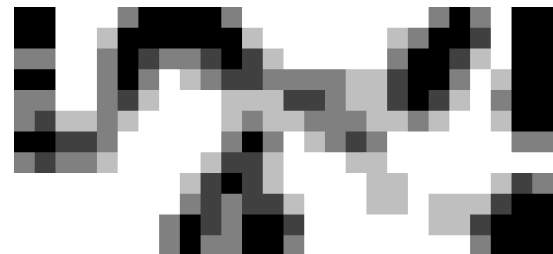
Table VII. EVALUATION OF THE TRAINED MODELS BY 10 FOLD CROSS-VALIDATION

Properties	A' Model	B' Model	C' Model
Instances	39000	9750	4000
CCI ^a	93,84%	95,68%	96,33%
FP rate	5,69%	5,42%	5,10%
FN rate	6,74%	3,44%	2,55%

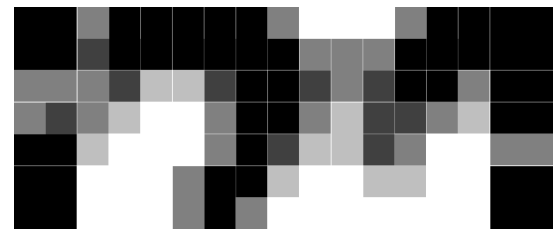
^aCorrectly Classified Instances



(a) Model A'.



(b) Model B'.



(c) Model C'.

Figure 7. Classification results of the different models.

V. CONCLUSION & FUTURE WORK

The results presented in section IV show that the classifier not only classifies correctly but also with a low false positive and false positive rate. The FP and FN rates in the experimental results are lower than in the training process. This could be due to the mixed images, where the PO and the sand are both often captured in a patch. The classifier has been trained to output a binary value when the input image is not posidonia (Class 1) or not posidonia (Class 0). Although this is a mistake, the final error in terms of classification is low, as has been seen in the table VII, and the classification is faster and simpler than if a lineal output model had been considered. Furthermore, the overlapping patches have allowed to output a set of four values of PO presence in the image.

Also the best classifier model has been chosen given the particularities of these images using Greedy stepwise method [15] in Weka, where LMT has been chosen. Moreover, the 314 possible attributes provided have been reduced up to four

Table VIII. EVALUATION OF THE TESTED MODELS

Properties	A' Model	B' Model	C' Model
Instances	107800	27500	9600
CCI ^a	98,71%	99,36%	99,55%
FP rate	2,21%	1,24%	0,88%
FN rate	0,38%	0,04%	0,02%

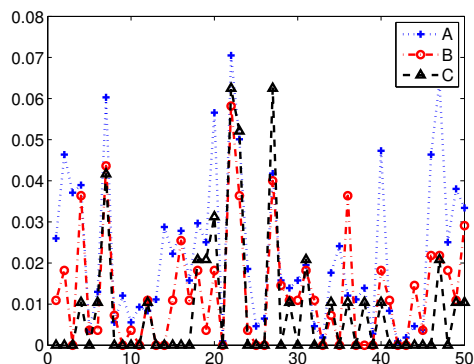
^aCorrectly Classified Instances

Figure 8. Classification results of 50 non PO images.

of them, fast and easy to calculate given an input image. The reduction has been done using a best subset algorithm provided also by Weka.

As future work, more than two classes should be considered, taking into account different algae species, rocks, and sand. Also, the acquisition of new images with better quality is necessary, as the ones used have noise coming from the analog readings transmitted through the underwater cable to the PC.

ACKNOWLEDGMENT

The authors would like to thank *Instituto Mediterráneo de Estudios Avanzados (IMEDEA)* for providing all the underwater images used in this work.

REFERENCES

- [1] J. M. González-Correa, J. T. Bayle, J. L. Sánchez-Lizaso, C. Valle, P. Sánchez-Jerez, and J. M. Ruiz, "Recovery of deep Posidonia oceanica meadows degraded by trawling," *Journal of Experimental Marine Biology and Ecology*, vol. 320, no. 1, pp. 65–76, Jun. 2005.
- [2] E. Diaz-Almela, N. Marbà, and C. M. Duarte, "Consequences of Mediterranean warming events in seagrass (*Posidonia oceanica*) flowering records," *Global Change Biology*, vol. 13, no. 1, pp. 224–235, Jan. 2007.
- [3] G. Arduzzone, A. Belluscio, and L. Maiorano, "Long-term change in the structure of a *Posidonia oceanica* landscape and its reference for a monitoring plan," *Marine Ecology*, vol. 27, no. 4, pp. 299–309, Dec. 2006.
- [4] D. Scaradozzi, G. Conte, G. De Capua, L. Sorbi, C. Luciani, P. De Cecco, and A. Sorci, "Innovative technology for studying growth areas of *Posidonia oceanica*," *2009 IEEE Workshop on Environmental, Energy, and Structural Monitoring Systems*, pp. 71–75, Sep. 2009.
- [5] L. Piazzzi, S. Acunto, and F. Cinelli, "Mapping of *Posidonia oceanica* beds around Elba Island (western Mediterranean) with integration of direct and indirect methods," *Oceanologica acta*, vol. 23, pp. 339–346, 2000.

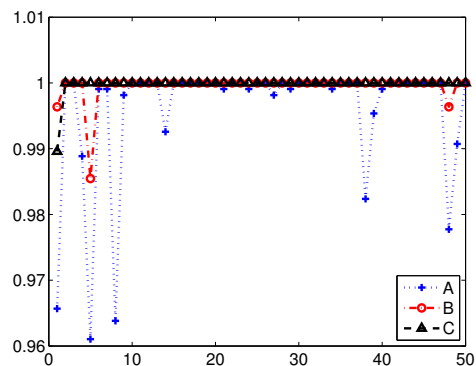


Figure 9. Classification results of 50 PO images.

- [6] R. Matarrese and M. Acquaro, "Applications of Remote Sensing Techniques for Mapping Posidonia Oceanica Meadows," *Geoscience and Remote Sensing Symposium, 2008. IGARSS 2008. IEEE International*, pp. 906–909, 2008.
- [7] a. Siccardi, R. Bozzano, and R. Bono, "Seabed vegetation analysis by a 2 MHz sonar," *Oceans '97. MTS/IEEE Conference Proceedings*, vol. 1, pp. 344–350, 1997.
- [8] V. Pasqualini, C. Pergent-Martini, G. Pergent, M. Agreil, G. Skoufias, L. Sourbes, and A. Tsirika, "Use of SPOT 5 for mapping seagrasses: An application to *Posidonia oceanica*," *Remote Sensing of Environment*, vol. 94, no. 1, pp. 39–45, Jan. 2005.
- [9] D. March, J. Alós, M. Cabanellas-Reboredo, E. Infantes, and M. Palmer, "Probabilistic mapping of *Posidonia oceanica* cover: A Bayesian geostatistical analysis of seabed images," *Aquatic Botany*, vol. 106, pp. 14–19, Apr. 2013.
- [10] A. Fornes, G. Basterretxea, A. Orfila, A. Jordi, A. Alvarez, and J. Tintore, "Mapping *posidonia oceanica* from IKONOS," *ISPRS Journal of Photogrammetry and Remote Sensing*, vol. 60, no. 5, pp. 315–322, Aug. 2006.
- [11] R. Haralick, K. Shanmugam, and I. Dinstein, "Textural features for image classification," *Systems, Man and Cybernetics, IEEE Transactions on*, vol. SMC-3, no. 6, pp. 610–621, 1973.
- [12] M. Hall, E. Frank, G. Holmes, B. Pfahringer, P. Reutemann, and I. H. Witten, "The weka data mining software: An update."
- [13] N. Landwehr, M. Hall, and E. Frank, "Logistic model trees," *Machine Learning*, pp. 1–54, 2005.
- [14] M. Hall, "Correlation-based feature selection for machine learning," Ph.D. dissertation, Department of Computer Science, University of Waikato, 1999.
- [15] T. H. Cormen, C. E. Leiserson, R. L. Rivest, and C. Stein, *Introduction to Algorithms*. MIT press, 2001.